JOURNAL OF MATERIALS SCIENCE 26 (1991) 6655–6672

Experiments on shear deformation, debonding and local load transfer in a model graphite/glass/epoxy microcomposite

R. GULINO*, P. SCHWARTZ, S. L. PHOENIX‡
Sibley School of Mechanical and Aerospace Engineering, Departments of Textiles and Apparel, and ‡Theoretical and Applied Mechanics, Cornell University, Ithaca, NY 14853, USA

Recent statistical theories for the failure of polymer matrix composites depend heavily on details of the stress redistribution around fibre breaks. The magnitudes and length scales of fibre overloads as well as the extent of fibre/matrix debonding are key components in the development of longitudinal versus transverse crack propagation. While several theoretical studies have been conducted to investigate the roles of these mechanisms, little has been substantiated experimentally about the matrix constitutive behaviour and mechanisms of debonding at the length scale of a fibre break. In order to predict the growth of transverse and longitudinal cracks using the same micromechanical model, we microscopically observed the epoxy shear behaviour around a single fibre break in a three-fibre microcomposite tape. The planar specimens consisted of a single graphite fibre placed between two larger glass fibres in an epoxy matrix. The interfibre spacing was less than one fibre diameter (< 6 μm) in order to reflect the spacing between fibres found in typical composites. The epoxy constitutive behaviour was modelled using shear-lag theory where the epoxy had elastic, plastic, and debond zones. The criteria for debonding were modified from conventional shear-lag approaches to reflect the orientational hardening in the epoxy network structure. The epoxy, which is brittle in bulk, locally underwent a shear strain of about 60% prior to debonding from the fibre.

1. Introduction

Recent statistical theories for the strength of a polymer matrix composite depend critically on the details of stress redistribution around fibre breaks [1–7]. The magnitudes and length scale of overloads in fibres adjacent to a cluster of contiguous breaks, combined with the strength statistics of the fibres at this characteristic length scale, determine the transverse growth of the cluster. The stress distribution at a break depends on the existence and growth of fibre/matrix debonding, which is often the precursor to longitudinal splitting [8–10]. While several theoretical studies have attempted to explain these phenomena [11–15], little has been substantiated experimentally about the constitutive behaviour and the mechanisms of debonding at the length scale of a fibre break, especially in the presence of other closely spaced fibres. In order to predict the onset of transverse and/or longitudinal crack propagation, and ultimately failure of a unidirectional composite, details of both the matrix constitutive behaviour around a cluster of broken fibres and the statistical strength of the fibres within this region must be known.

Currently the most widely applied methods for determining the load transfer capabilities of a particular fibre/matrix system are the pull-out [16, 17] and the single-filament-composite techniques [18, 19]. Although these techniques have greatly advanced the understanding of the fibre/matrix interface, the resulting models for the matrix constitutive behaviour are not sufficiently detailed for the construction of accurate shear-lag models of load transfer.

In particular, the single-filament-composite technique, provides an estimate of the average interfacial shear strength of the fibre/matrix system from a knowledge of the final fragment length distribution and the fibre strength statistics. Inherent difficulties, however, involve (i) a lack of precise knowledge of the fibre strength statistics at the length scale of the mean fragmentation length, and (ii) a lack of realism in the matrix stress field around one isolated fibre as the matrix must carry not only shear but also significant tensile loads.

Epoxies used in composites typically behave as brittle materials when tested in bulk, with a tensile strain to failure ranging from 2%–4%. Yet, as shown by Glad [20] in experiments on thin epoxy films, on a much smaller scale epoxies can undergo large plastic deformations. If the strength of the fibre/matrix interface exceeds the yield stress in the epoxy, then the

* *Present address*: Applied Remote Technology, 9950 Scripp's Lake Drive, Suite 106, San Diego, CA 92131, USA.

0022–2461/91 $03.00 + .12

shear profile around a fibre break will exhibit a plastic region. Glad showed that the extent of this plastic region is limited by severe orientation hardening of the epoxy network. Thus debonding will occur unless an alternative mechanism, such as transverse crack propagation, develops near the fibre break thus relieving the shear deformation in the matrix. The fibre/matrix system chosen for this research did not initially develop a transverse matrix crack [18] and therefore could be modelled using shear-lag theory where the epoxy along the fibre had elastic, plastic, and debond zones. We found that the criteria for debonding had to be modified from conventional shear-lag approaches to account for extensional deformation bridging the fibre break region.

In the present study, the epoxy shear behaviour around a single graphite fibre break was investigated by observing microscopically the load transfer region surrounding the break where the shear pattern was observed using photoelastic methods. The matrix deformation was constrained as in conventional high-volume-fraction composites. This constraint was achieved by closely placing a glass fibre on each side of the graphite fibre in an epoxy to form a planar tape, as shown in Fig. 1. Glass fibres were chosen because their strain to failure is about twice that of graphite fibres. Samples were carefully produced under controlled conditions to reduce unwanted variability. Moreover, this technique estimated the load transfer characteristics of the fibre/matrix interface without requiring knowledge of the local fibre strength as in the single-filament-composite technique [18, 19]. In fact, the fibre strength statistics, at the length scale of load transfer, were estimated as a secondary result of the technique; the method is discussed in a companion paper [21].

The samples were stressed to preset levels, and the numbers and positions of the breaks in the graphite fibre were recorded at each level. Concurrently, each break was viewed at high magnification in a plane polariscope while under load. Measurements were made to characterize the load recovery of the graphite fibre. The measurements on load transfer were used in conjunction with a shear-lag model to deduce the matrix constitutive behaviour.

2. Specimen fabrication

The technique for fabricating and testing the microcomposite samples is described in detail in Gulino and Phoenix [21] and in Gulino [22]. Here we give only a brief summary.

2.1. Materials

The three-fibre microcomposites were composed of IM-6 graphite fibres (Hercules), SK glass fibres (Owens Corning Fiberglas), and DER 331/DEH 26 epoxy system (Dow Chemical). The graphite fibres were surface treated by the manufacturer, but not coated with a surface finish, and we extracted them from a 12000 filament tow. Their nominal strain to failure was in the range 1%–2%, and they had an average modulus of elasticity of 280 GPa. The as-received SK glass fibres were coated with an epoxy compatible, proprietary sizing, P365A, and we extracted them from a 204 filament strand. These fibres had a nominal strain to failure of from 3%–5%, and an average elastic modulus of 90 GPa. The epoxy resin (DER 331) was diglycidyl ether of bisphenol A (DGEBA) with a resin molecular weight of 374. The hardening agent (DEH 26) was tetraethylene pentamine (TEPA), an aliphatic polyamine. ASTM standard epoxy "dogbone" specimens were fabricated, from which an initial modulus of 2.80 GPa was determined, in agreement with values obtained on similar epoxies. Using a Babinet–Soleil compensator, the material fringe value was measured over three fringe orders, covering the range 0%–1% strain.

2.2. Microcomposite fabrication

The formidability of fabricating the microcomposite tapes can be appreciated by first reviewing their physical size. The dimensions of the three-fibre microcomposites were 40 mm long (20 mm gauge length), 200 μm wide, and 50 μm thick (Fig. 1). The graphite and glass fibres were 5.5 and 13 μm diameter, respectively. The interfibre spacing was to be held at 3 μm with a deviation of less than 1 μm over the sample length. Consequently, the fabrication of the samples required special techniques using micropositioners and optical microscopes.

The procedure for the fabrication of the microcomposites was broken down into a few basic tasks. The fibres were extracted from their yarns, aligned in the desired tape configuration, and embedded in an epoxy film as shown in Fig. 2. The microcomposite initially contained five fibres. The desired sample was composed of the three centre fibres, while the two additional fibres formed the edges of the epoxy film, thus controlling the effects of the liquid epoxy surface tension which would have otherwise destroyed the uniform spacing of the three centre fibres. Next the undesired edge sections of the sample were removed, producing the cross-sectional shape already shown in Fig. 1. (See also Figs 6 and 7 of Gulino and Phoenix

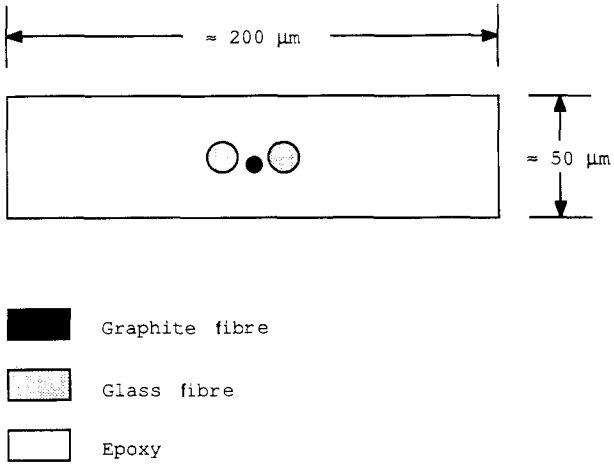

Figure 1 Cross-sectional view of a microcomposite tape showing nominal dimensions.

[21]). The resulting three-fibre microcomposite tape was tabbed by sandwiching each end between a square steel wafer, covered by a thin layer of adhesive, and a thin cardboard frame. The steel wafers minimized the deformation in the clamp region, and provided a hard flat region for attaching the sample to the load frame.

2.3. Summary of sample properties

Two three-fibre microcomposite samples, subsequently referred to as samples 11 and 12, were fabricated and tested. The geometrical properties of samples 11 and 12 are shown in Table I. The equivalent volume fraction for a three-dimensional composite was computed assuming a uniformly spaced hexagonal array of fibres. The equivalent volume fraction for a planar tape was computed assuming the thickness of the tape was equal to the diameter of the graphite fibre. The volume fractions produced are in the range of typical commercial composites, namely 30%–70%.

After testing, samples 11 and 12 were sectioned to measure the matrix area and the interfibre spacing at various positions along the specimen. The values of the matrix area and spacing are shown in Tables II and III, for samples 11 and 12, respectively. Modelling each section as a spring in series with the other sections, the deviation from the nominal strain was computed. In sample 11, the deviation from the nominal strain (expressed as a percentage of the nominal strain) was 5% or less. Sample 12, on the other hand, had a deviation of nearly 10% at each end, and due to this deviation, the breaks occurring within these end regions were not selected for detailed analysis.

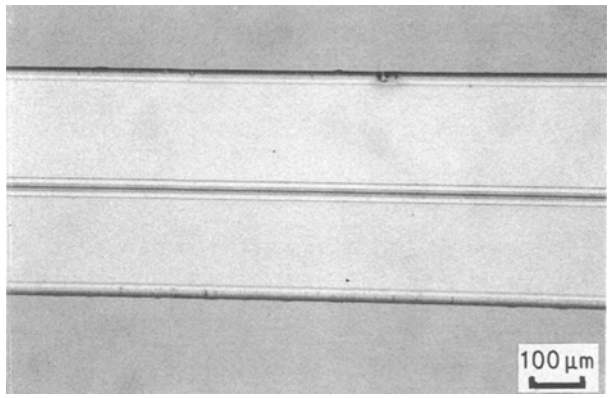

Figure 2 Top view of original five-fibre microcomposite tape with two outside glass fibres used to control epoxy surface tension effects after dipping.

TABLE I Summary of the geometric properties of samples 11 and 12

Sample no.	Length (mm)	Graphite fibre diameter (μm)	Average spacing (μm)	Equivalent volume fraction (hexagonal array) (%)	Equivalent volume fraction (tape) (%)
11	19.62	5.5	3.1	37	50
12	19.69	5.5	2.8	40	52

TABLE II Summary of the measurements taken at different sections along sample 11

Position along fibre (mm)	Area of matrix (10^{-3} μm^2)	Spacing glass/graph (μm)	Spacing graph/glass (μm)	Deviation from nominal strain (%)
2.5	13.2	2.7	2.9	5
7.6	14.8	2.7	3.2	− 2
12.7	15.5	3.2	3.2	− 5
17.8	13.8	3.4	3.6	2
Average	14.3	3.0	3.2	

TABLE III Summary of the measurements taken at the different sections along sample 12

Position along fibre (mm)	Area of matrix (10^{-3} μm^2)	Spacing glass/graph (μm)	Spacing graph/glass (μm)	Deviation from nominal strain (%)
0.6	9.7	2.3	2.7	− 10
5.7	8.1	2.5	2.7	− 1
10.7	8.2	2.3	3.1	− 1
15.8	7.4	2.2	3.9	3
18.4	6.8	1.6	3.6	7
Average	8.0	2.2	3.2	

2.4. The load frame

The load frame was built specifically to apply a uniform strain to the microcomposite tape such that each break could be located and observed through a microscope. To accomplish this task, a low-profile load frame was constructed which could be mounted on the stage of an inverted metallographic microscope. A special fixture was made that enabled a sheet polarizer to be placed between the sample and the microscope objective. The addition of the sheet polarizer allowed the sample to be viewed using a plane polariscope. The microscope was equipped with photographic attachments to record the photoelastic patterns. A dial gauge, held against the microscope stage, was used to determine the location of the fibre breaks along the specimen axis.

3. Shear-lag model for the load transfer around a single graphite fibre break

As the applied strain is increased in the three-fibre microcomposite, the centre graphite fibre eventually breaks at a flaw. There, the graphite fibre retracts locally, producing a shear force in the epoxy, but at some distance from the break the graphite fibre maintains the level of applied strain. The resulting load-recovery length and the associated shear profile depend on the epoxy shear behaviour, the strength of the graphite fibre/epoxy interface, the elastic properties of the fibres and epoxy, and the local fibre/epoxy volume fraction. Further increases in the applied strain result in additional graphite fibre breaks, until the fragment lengths are too small to achieve further increases in stress within the central portion of some fragment. The number of fibre breaks as a function of the applied strain is the subject of a previous paper [21], while the matrix shear behaviour and the growth and onset of debonding will be the subject of this paper. In order to motivate the degree of complexity required in the shear-lag model, the constitutive behaviour of the epoxy in tension is discussed.

3.1. Microdeformation and network structure of epoxy

The large tensile deformation of epoxy was investigated recently by Glad [20]. He conducted a series of experiments on the microdeformation of thin (1–2 μm) epoxy films composed of methylenedianilene (MDA) cross-linked DGEBA epoxies with a range of total strand densities, where the total strand density is a sum of the entanglement and cross-linked strand densities. The films were bonded to a copper grid and deformed in uniaxial tension to produce plane stress deformation zones. These deformation zones were viewed as micronecks in the epoxy film and the thickness profiles of the shoulders were measured by quantitative transmission electron microscopy. These profiles were used to calculate a true stress–true strain curve in tension and at a constant strain rate, under the assumption that the deformation was volume preserving and produced by a state of uniform uniaxial tension with little lateral contraction in the plane. (Note that because of the localization of the necking in the film geometry, the deformation was associated primarily with contractions through the thickness, with little transverse contraction in the plane). The stress–strain behaviour was computed beyond the yield point, and typically consisted of a small region of strain softening, gradual strain hardening, and finally a region of rapid strain hardening, where network effects dominated the deformation up to fracture.

The stress–strain curves for epoxies have two important features. First, epoxy can undergo large deformations within small regions whose length scale is of the order of 100 μm, contrary to the brittle fracture observed in large samples, where the length scale is of the order of 100 mm. These large deformations form a relatively flat plastic region in the stress–strain curve. Second, the large deformations are limited by the network structure of the epoxy. Thus, after significant deformation, the epoxy suddenly strain hardens, and ultimately fractures when reaching a critical extension ratio, λ_c, which is related [20] to the maximum extension ratio, λ_{max}, defined as the maximum extension ratio of a single network strand. The extension ratio, λ, is defined as the ratio of the deformed to the undeformed length.

Fig. 3 shows a stress–strain curve of the epoxy shear stress as a function of the first principal extension ratio approximated from the film experiments of Glad [20]. Fig. 3 also shows a corresponding simplified model for the effect of the epoxy on the fibre as was used in the shear-lag analysis. The expeimental constitutive behaviour of an epoxy element between the fibres was approximated by three different zones with four associated constants: the yield extension ratio, λ_{yield}, the average shear stress in the plastic region, $\tau_{plastic}$, the debond extension ratio, λ_{debond}, and the residual frictional stress in shear, τ_{debond} (resulting in part from compressive interfacial stresses due to epoxy shrinkage during curing). Initially ($\lambda < \lambda_{yield}$), the matrix was modelled as a linearly elastic material. Note that

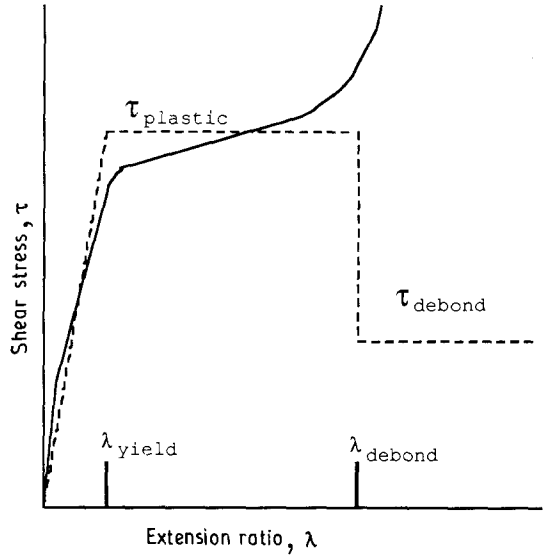

Figure 3 (---) Simplified constitutive model used in the shear-lag analysis compared with (——) an approximation of the shear behaviour derived from experiments by Glad [20].

the shear modulus can be determined by λ_{yield}, $\tau_{plastic}$, and Poisson's ratio, ν. In the next zone ($\lambda_{yield} \leqslant \lambda < \lambda_{debond}$), the matrix was modelled as perfectly plastic, where the shear stress was approximated by the average stress in the mildly strain-hardening region. This zone was applicable within the range of deformation from the yield extension ratio to the debond extension ratio. In the region of strong orientational hardening ($\lambda_{debond} \leqslant \lambda$), a small increase in strain corresponds to a very large increase in stress. Thus, the criteria for the initiation of debonding was modelled in terms of a limiting strain, rather than a maximum stress. Assuming that the strength of the interface is sufficient to sustain large plastic deformation in the epoxy, the critical extension ratio, which for purposes here is taken as λ_{debond}, has a greater effect on the debond zone length than the ultimate strength of the graphite/epoxy interface. After debonding there is some residual shear stress, which has been approximated by the constant τ_{debond} in the model presented here.

Assuming that the matrix deformation between the graphite and glass fibre can be modelled as simple shear, the deformation is by definition volume preserving where the principal extension ratios are $\lambda_1 = \lambda$, $\lambda_2 = 1$, $\lambda_3 = 1/\lambda$, and the shear strain is related to the principal extension ratio by [22]

$$\gamma = \lambda - 1/\lambda \quad (1)$$

3.2. Influence of the extensional strain near the fibre break on the model shear-lag parameters

As previously stated, the critical extension ratio is determined by the network structure of the epoxy. When a fibre breaks in the strained microcomposite, either a transverse crack forms in the matrix at the break, or two longitudinal interfacial cracks, called the debond zones, form symmetrically along the fibre on each side of the break. In this particular fibre/matrix system debonding occurs as was demonstrated by Netravali *et al.* [18]. As shown in Fig. 4, the matrix within the two debond zones and bridging the fibre break undergoes not only a shear strain, but also an extensional strain parallel to the fibre (in addition to the nominal axial strain, ε, of the sample). From geometrical considerations, for a given end separation this extensional strain must grow unbounded as the debond zone length shrinks to zero. From Mohr's circle considerations, for a shear strain superimposed on a longitudinal strain of the same order, the limiting shear strain required to approach the critical extensional strain in the epoxy network is significantly reduced. Thus, close to the fibre break in the debond zone, the limiting shear strain is reduced, as indicated in Fig. 4. Hence the limiting shear strain is a function of position along the fibre. As the debond zone length becomes large, the debond shear strain increases to a constant value. This value will be termed the far-field debond shear strain, γ^*_{debond}.

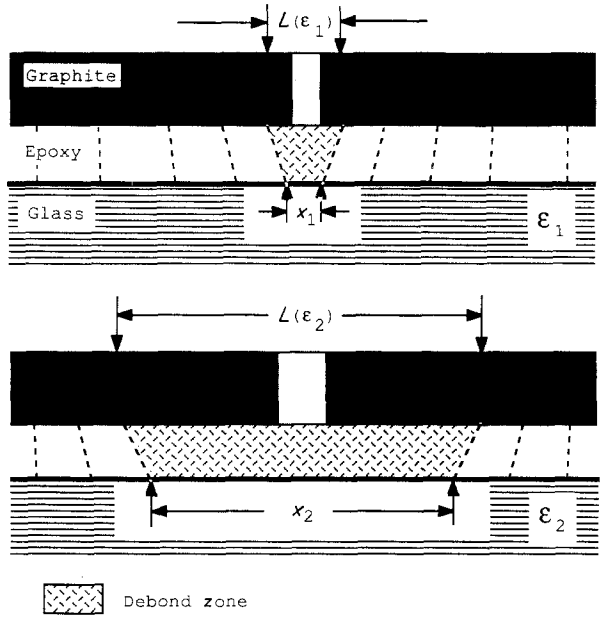

Figure 4 Debond zone length at two levels of strain, showing a decrease in the extensional strain of the matrix near a break as the debond length grows, where x is the length of the undeformed debond zone, and L that of the debonded zone. For $\varepsilon_2 > \varepsilon_1$, the approximate extensional strain in the matrix is $L(\varepsilon_2)/x_2 < L(\varepsilon_1)/x_1$.

3.3. Displacement formulation of the shear-lag model

To characterize the load transfer regions of a fragment within the three-fibre microcomposite under nominal strain ε, a fragment of arbitrary but finite length was modelled. (Dependence on ε is generally suppressed in the notation.) The complexity of this task was significantly reduced by employing the symmetry of the microcomposite tape. First, the microcomposite was symmetric about the graphite fibre axis. In addition, each fragment was symmetric about the transverse plane through its midpoint, as shown in Fig. 5. The load recovery of the graphite fibre from the position of the break was computed using the shear-lag assumptions and by assuming that the fibre/matrix interaction could be modelled by an idealized elastic/plastic/debonding constitutive model for the matrix. The influence of the extensional strain near the fibre break on the debond shear strain was incorporated indirectly by making the debond shear strain a function of the applied strain. The solution was obtained using a displacement formulation as follows.

Referring to Figs 5–7, we let x be the position along the graphite fibre with origin at the break, and let $u(x)$ and $w(x)$ be the longitudinal displacements of the graphite and glass fibres, respectively. The corresponding normalized displacements with respect to the fibre diameter, D_c, are $U(\xi) = u/D_c$ and $W(\xi) = w/D_c$ where $\xi = x/D_c$. The equation of equilibrium was obtained by balancing the forces in the axial direction from the free body diagram of a fibre element, Fig. 6. The general equation for equilibrium in the axial direction is

$$\frac{dP_i}{dx} - h_{i-1,i}\tau_{i-1,i} - h_{i,i+1}\tau_{i,i+1} = 0 \quad (2)$$

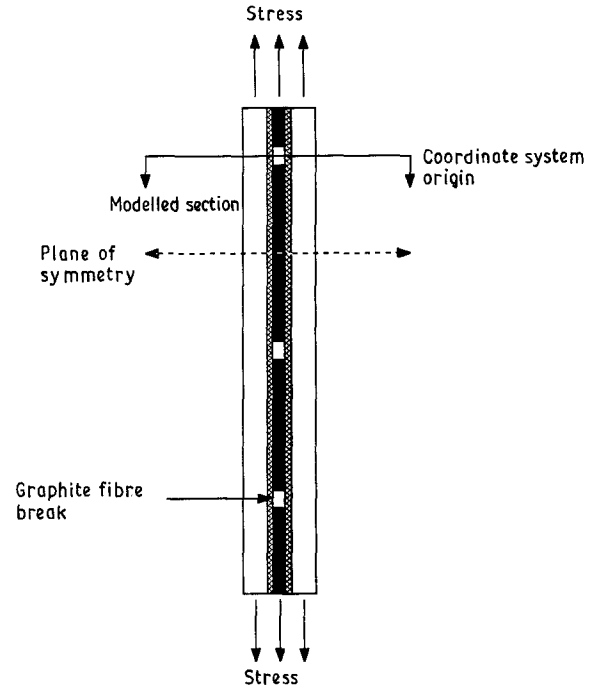

Figure 5 Boundary of representative section to be modelled using shear-lag assumptions.

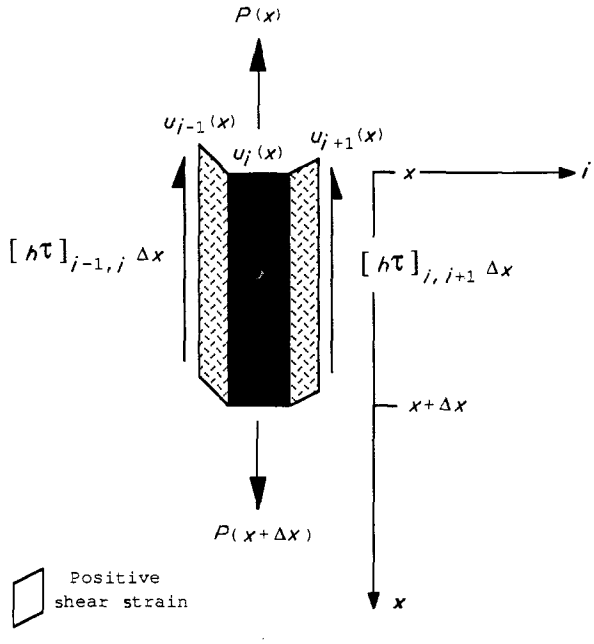

Figure 6 Free-body diagram of the forces in the axial direction under shear-lag assumptions.

where P_i is the fibre tensile force, $\tau_{i-1,i}$ is the matrix shear stress, $h_{i-1,i}$ is the effective shear transfer width between fibres $i-1$ and i, which alternate as graphite and glass.

In terms of displacements, the constitutive laws for the graphite and glass fibres are, respectively

$$P_c = (AE)_c \, dU/d\xi \tag{3}$$

and

$$P_g = (AE)_g \, dW/d\xi \tag{4}$$

where $(AE)_c$ and $(AE)_g$ are the stiffnesses, with respect to strain, of the graphite and glass fibres, respectively, A being area and E being elastic modulus.

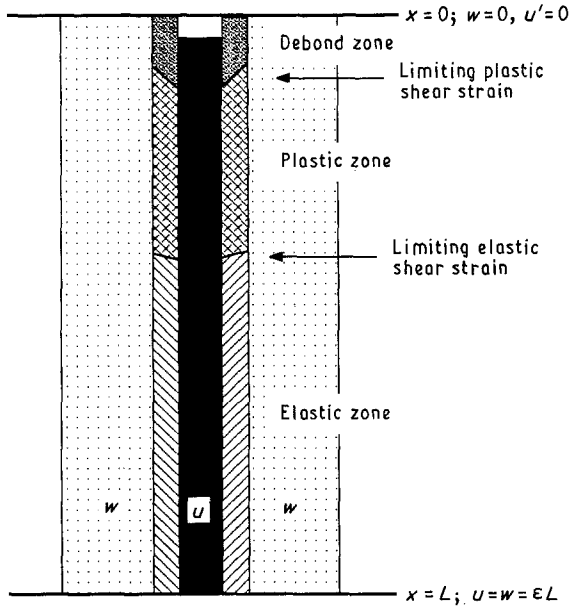

Figure 7 Modelled section of three-fibre microcomposite.

The constitutive law for the matrix has been formulated in accordance with three zones along the graphite fibre as shown in Fig. 7: the debond zone, the plastic zone, and the elastic zone. First we define the shear strain as

$$\gamma(\xi) = \frac{u\xi - w\xi}{s} = \frac{U(\xi) - W(\xi)}{\psi} \tag{5}$$

where s is the effective interfibre spacing and $\psi = s/D_c$. We let L be the fragment half-length and let $\Lambda = L/D_c$. We let x_{yield} be the transition point between the plastic and elastic zones and let $\mu = x_{yield}/D_c$, being defined by $\gamma(\mu) = \gamma_{yield}$ where γ_{yield} is the epoxy yield strain in shear. We also let x_{debond} be the transition point between the debond zone and the plastic zone and let $\eta = x_{debond}/D_c$ where the transition is defined by $\gamma(\eta) = \gamma_{debond}$. Thus the constitutive law for the matrix is cast as

$$\tau = \begin{cases} \tau_{debond} & 0 \leqslant \xi \leqslant \eta \\ \tau_{yield} & \eta < \xi \leqslant \mu \\ G\gamma & \mu < \xi \leqslant \Lambda \end{cases} \tag{6}$$

where G is the elastic shear modulus.

The effective shear transfer width, h, is taken to be equal in the plastic and debond zones and is denoted by h_p; in the elastic zone h is denoted as h_e.

Application of the general governing differential equation to each zone yields a pair of coupled differential equations for each zone. Differentiation by ξ is represented by a prime. The full set of equations is

$$\left.\begin{aligned} W'' - \alpha\tau_{debond} &= 0 \\ U'' - \beta\tau_{debond} &= 0 \end{aligned}\right\} \quad \text{for } 0 \leqslant \xi \leqslant \eta \tag{7}$$

$$\left.\begin{aligned} W'' - \alpha\tau_{yield} &= 0 \\ U'' - \beta\tau_{yield} &= 0 \end{aligned}\right\} \quad \text{for } \eta < \xi \leqslant \mu \tag{8}$$

and

$$\left.\begin{aligned} W'' + 2\phi(U - W) &= 0 \\ U'' + 2\theta(W - U) &= 0 \end{aligned}\right\} \quad \text{for } \mu < \xi \leqslant \Lambda \quad (9)$$

where

$$\phi = \frac{Gh_eD_c}{2\psi(AE)_g} \quad (10)$$

$$\theta = \frac{Gh_eD_c}{\psi(AE)_c} \quad (11)$$

$$\alpha = \frac{h_pD_c}{2(AE)_g} \quad (12)$$

and

$$\beta = \frac{h_pD_c}{(AE)_c} \quad (13)$$

The boundary conditions for the broken graphite fibre in the microcomposite are shown in Fig. 7. Continuity of displacements and internal equilibrium in each fibre are used to find the boundary conditions linking the three zones together. At $\xi = \Lambda$, the line of symmetry of the fragment (of total length $2L$) we have

$$\begin{aligned} U(\Lambda) &= W(\Lambda) \\ &= \varepsilon L/D_c \end{aligned} \quad (14)$$

where ε is the applied strain. At both the elastic–plastic boundary, $\xi = \mu$, and the plastic–debond boundary, $\xi = \eta$, we have continuity in $U(\xi)$, $U'(\xi)$, $W(\xi)$ and $W'(\xi)$. At the fibre break, $\xi = 0$, the strain in the graphite fibre must be zero, so that $U'(0) = 0$. By symmetry $W(0) = 0$ for the glass fibre, whereas $U(0)$ and $W'(0)$ must be determined from the solution.

Solution is straightforward and the results are

$$\left.\begin{aligned} U(\xi) &= A_1 + \beta\tau_{debond}\xi^2 \\ W(\xi) &= E_1\xi + \alpha\tau_{debond}\xi^2 \end{aligned}\right\} \quad 0 \leqslant \xi \leqslant \eta \quad (15)$$

$$\left.\begin{aligned} U(\xi) &= A_2 + 2\beta\eta(\tau_{debond} - \tau_{yield}) + \beta\tau_{yield}\xi^2 \\ W(\xi) &= -\alpha\eta^2(\tau_{debond} - \tau_{yield}) + E_2\xi + \alpha\tau_{yield}\xi^2 \end{aligned}\right\} \quad \eta < \xi \leqslant \mu \quad (16)$$

and

$$\left.\begin{aligned} U(\xi) &= \varepsilon\Lambda - K(\Lambda - \xi) + \theta T\sinh[m(\Lambda - \xi)] \\ W(\xi) &= \varepsilon\Lambda - K(\Lambda - \xi) + \phi T\sinh[m(\Lambda - \xi)] \end{aligned}\right\} \quad \mu < \xi \leqslant \Lambda \quad (17)$$

where

$$m = [2(\phi + \theta)]^{1/2} \quad (18)$$

$$\begin{aligned} T = {} & [\alpha\eta^2(\tau_{debond} - \tau_{yield}) + \alpha\tau_{debond}\mu^2 + \varepsilon\Lambda \\ & - 2\beta\eta(\tau_{debond} - \tau_{yield}) - 2\Lambda\beta\mu\tau_{debond}]/ \\ & \{\mu(\phi\mu + \theta\Lambda)\cosh[m(\Lambda - \mu)] \\ & + \phi\sinh[m(\Lambda - \mu)]\} \end{aligned} \quad (19)$$

$$\begin{aligned} K = {} & Tm\theta\cosh[m(\Lambda - \mu)] + 2\beta\eta \\ & \times(\tau_{debond} - \tau_{yield}) + 2\beta\mu\tau_{yield} \end{aligned} \quad (20)$$

$$E_2 = Tm\phi\cosh[m(\Lambda - \mu)] + K - 2\alpha\mu\tau_{yield} \quad (21)$$

$$\begin{aligned} A_2 = {} & T\theta\cosh[m(\Lambda - \mu)] - K(\Lambda - \mu) + \varepsilon\Lambda \\ & - 2\beta\eta\mu(\tau_{debond} - \tau_{yield}) + \beta\mu^2\tau_{yield} \end{aligned} \quad (22)$$

$$E_1 = E_2 - 2\alpha\eta(\tau_{debond} - \tau_{yield}) \quad (23)$$

and

$$\begin{aligned} A_1 = {} & A_2 + 2\beta\eta^2(\tau_{debond} - \tau_{yield}) \\ & - \beta\eta^2(\tau_{debond} - \tau_{yield}) \end{aligned} \quad (24)$$

The above analytical results are the basis for interpreting the experimental results discussed later, and for estimating values for the key parameters.

4. Testing the microcomposites

During testing, a microcomposite tape was clamped into a load frame, and then loaded at a constant elongation rate to a specific load level. The nominal load levels were determined by obtaining the initial modulus of the samples and then computing the loads corresponding to 0.1% increments of strain. At each load level, the numbers of breaks and their positions in the sample were recorded. At selected breaks, measurements were made to characterize the load transfer. Because the matrix was undergoing mild load relaxation while the measurements were being made, the sample was unloaded and allowed to recover at no load for at least twice the time period that it was under load. The type of measurements, how they were made, the errors in making the measurements, and the data gathered are discussed in the following sections.

4.1. Measurement of the applied longitudinal strain

A crucial aspect was to be able to determine accurately the strain in a specimen, because the load transfer around a break in the graphite fibre strongly depends on the longitudinal strain, ε. It is therefore critical to be able to determine accurately the residual strain in the samples. The residual strain after fabrication was obtained from an analysis of the microcomposite fabrication process, including fibre pretensioning and thermal contraction of the aluminium dipping frame during cooling. An expression for the residual strain, ε_r, was derived in Gulino [23] and is

$$\varepsilon_r = \left[1 - \frac{(AE)_f}{(AE)_t}\right] \times \left[\frac{P_0}{(AE)_f} - (\alpha_m - \alpha_{al})(T_c - T_o)\right] \quad (25)$$

where $(AE)_t$ is the stiffness of the microcomposite, $(AE)_f$ is the stiffness of the fibres, P_0 is the total pretension load applied to the fibres during alignment, α_{al} is the linear thermal coefficient of expansion of the aluminium dipping frame, α_m is the linear thermal

coefficient of expansion of the epoxy matrix, T_c is the cure temperature and T_o is the room temperature.

In the above equation, the microcomposite stiffness was computed from the initial slope of the load–elongation curve, compensated for the stiffness of the load cell. The stiffness of the glass fibres was obtained from a proof test on that particular fibre. The stiffness of the graphite fibre was computed from the measured area of the fibre and the average modulus of a graphite fibre. The stiffness of the matrix was computed from the area of the epoxy, measured from microcomposite cross-sections, and the epoxy modulus. The measured microcomposite stiffness was within 1% of the stiffness computed by summing all the component stiffnesses.

The residual strain in the graphite fibres was computed to be about 0.05% which is not significant considering the accuracy of the model and in comparison to the accuracy of applied strain measurement. Table IV gives the values of the variables used in the calculation.

The tensile strain, ε, applied to a microcomposite sample was determined by three different methods. The first and most accurate method involved computing the strain using the relative displacements of the ends of the sample; the finite stiffness of the load cell was accounted for, but any deformation in the sample tabs was neglected. This assumption was verified through tension tests on the SK glass fibres which displayed no measurable reduction in stiffness up to failure at 3%–5% strain. The second method computed the strain from the relative positions of the breaks as a function of load. These positions were known to be within 30–60 μm (five to ten fibre diameters) and while less accurate, the results were consistent with those from the first method. In the third method, the strain was computed by using the initial modulus of the sample. This method was accurate at low loads, but produced deviations as the matrix stress–strain rule became non-linear beyond 2% strain.

4.2. Photoelastic patterns

The epoxy matrix was stress birefringent, or photoelastic, and thus the load recovery could be visualized by observing the sample through crossed polarizers. The intensity of monochromatic light, I, passing through a photoelastic material in a plane polariscope is [24]

$$I = B\sin^2(2\alpha)\sin^2(\Delta/2) \quad (26)$$

where B is a constant, α here is the angle between the principal stress direction and the axis of polarization. The relative retardation is

$$\Delta = \frac{2\pi tq}{\lambda}(\sigma_1^* - \sigma_2^*) \quad (27)$$

where λ is the wavelength of the light, q is the relative stress-optic coefficient, $(\sigma_1^* - \sigma_2^*)$ is the difference in the principal in-plane stresses, and t is the thickness of the material.

The photoelastic patterns observed around each graphite fibre break can be understood by dividing the microcomposite through its thickness into three layers, where the state of stress in each layer consists primarily of a single type of deformation as indicated in Fig. 8. The first layer consists of a sheet of epoxy under uniform tension parallel to the fibres. The second layer contains the fibres and the epoxy between the fibres, where the epoxy between the fibres undergoes, primarily, simple shear. The epoxy outside the fibres is under uniform tension. The third layer, like the first, consists of a sheet of epoxy under uniform tension. Thus for the first and third layers, the axis of polarization is parallel to the principal stress axis, $\alpha = 0$ in Equation 26, and thus, these layers do not contribute to the photoelastic pattern. Regions of the second layer of epoxy, those in shear, produced the photoelastic pattern. It is important to note that the relative retardation is not infuenced by the value of α.

The relative retardation is often quantified in terms of the retardation between sequential extinctions

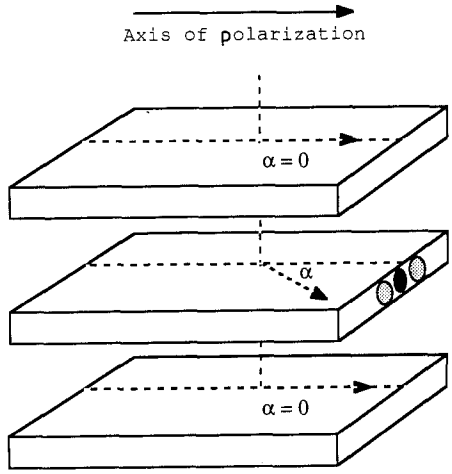

Figure 8 Conceptual division of a microcomposite tape into three layers showing (– – →) principal stress direction with respect to (———) direction of loading, which is colinear with the axis of polarization.

TABLE IV Summary of the computation of the residual strain in samples 11 and 12

Sample no.	Linear coefficient of thermal expansion		Stiffness in fibres (N)	Stiffness ratio fibre/sample	Room temperature (°C)	Cure temperature (°C)	Post-curing strain in fibres (%) (+ tension)
	Epoxy (10^{-6} °C^{-1})	Aluminium (10^{-6} °C^{-1})					
11	68	23	27.9	0.41	24	80	0.05
12	68	23	28.1	0.56	24	80	0.04

(dark fringes), known as one fringe order. The fringe order, N, is

$$N = \frac{\Delta}{2\pi} \tag{28}$$

and can be expressed in terms of the in-plane shear strain by

$$N = \frac{2t\gamma}{f_s/G} \tag{29}$$

where γ is the principal in-plane shear strain, f_s is the material fringe value, G is the shear modulus of the material, and t is the thickness of the strained material.

When polychromatic light is used, the amount of relative retardation will produce transmitted light of a characteristic colour. Table V displays the characteristic sequence of colours corresponding to increasing stress, or fringe order. Up to $N = 0.5$, the colour associated with the fringe value is difficult to differentiate from white. To increase the resolution within this range, a full wave plate was inserted into the plane polariscope. The full wave plate has a fringe order of 1. Thus the value of the fringe order associated with a particular value of shear stress is shifted by 1, which moves low values of fringe order, 0–0.5, into the area of maximum colour variation.

The material fringe value was determined in the linear elastic region of the epoxy constitutive behaviour, yet the deformation in the epoxy surrounding the graphite fibre was well past the epoxy elastic limit. In order to interpret the observed fringe orders, the material fringe value was converted from stress to strain using the elastic shear modulus. This value was assumed to apply to strains far in excess of the elastic limit. This assumption does not allow precise evaluation of the strain in the epoxy from the observed fringe order, and therefore, the photoelastic patterns were used only in a qualitative sense.

4.3. Load-transfer characterization in the three-fibre microcomposites

Visualization of the load transfer through photoelasticity enabled four measurements to be made at each selected break in the graphite fibre. These measurements were the separation between the ends of the fibre, the length of the debond zone, the length of the photoelastic pattern starting from the debond zone, termed the birefringence length, and the colour of the maximum fringe order observed for each strain level. These measurements are shown in an illustration of the load-recovery region as described by the shear-lag model, Fig. 9. The data contained error in both the measurement of the length and of the corresponding value of the applied strain.

4.3.1. Measurements of the graphite/epoxy load transfer

For ease of comparison, the length measurements were normalized by the diameter of the graphite fibre, D_c. The separation between the ends of the fibres was measured while observing the breaks with unpolarized light. The observed pattern is represented in Fig. 10. Although numerous photographs were taken of the end separation, none retained the same clarity as when viewed directly through the microscope.

The length of the debond zone was identified by a sharp drop in the fringe order as the graphite/epoxy interface began to fail. The growth of the debond zone can be seen in Figs 11 and 12. These photographs were

TABLE V Fringe orders and the corresponding observed colour for polychromatic light

Fringe order	Colour
0	Black
0.07	Iron grey
0.17	Lavender grey
0.27	Grey–blue
0.38	Clear grey
0.45	White
0.49	Straw yellow
0.53	Light yellow
0.58	Bright yellow
0.75	Brown yellow
0.88	Red–orange
0.93	Red
0.98	Purple
1.02	Indigo
1.15	Sky blue
1.27	Green–blue
1.30	Green
1.44	Light green
1.47	Yellow–green
1.51	Green–yellow
1.58	Yellow
1.65	Orange
1.74	Orange–red
1.91	Violet–red

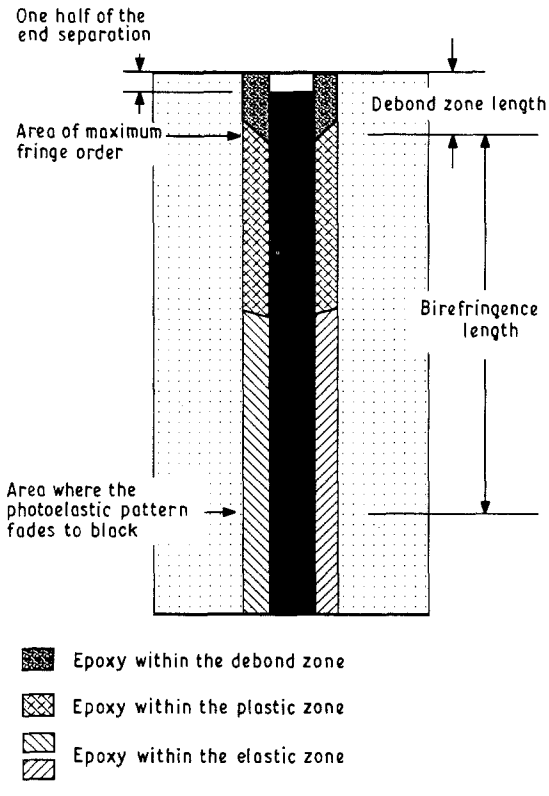

Figure 9 Depiction of load-transfer measurements on the shear-lag model.

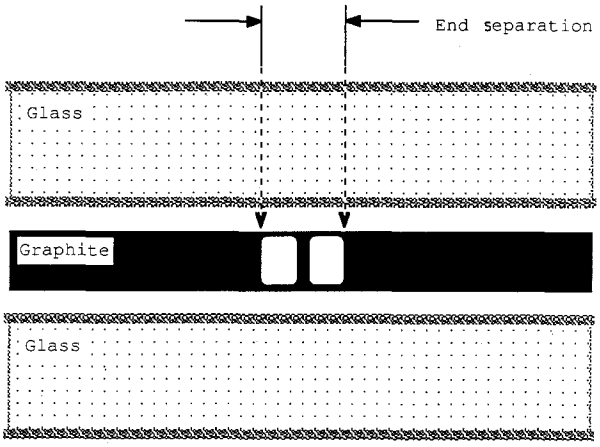

Figure 10 Pictorial representation of the end separation at a break in a microcomposite as seen with unpolarized light.

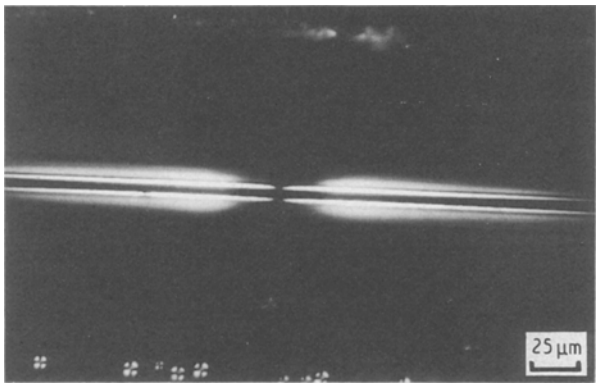

Figure 11 Break in a three-fibre microcomposite viewed through cross polarizers at 2.34% strain.

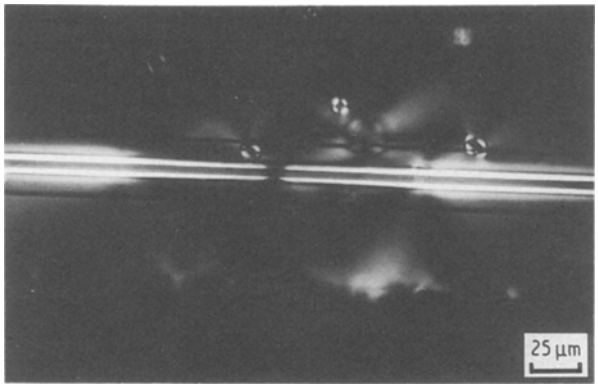

Figure 12 Break in a three-fibre microcomposite viewed through cross polarizers at 2.99% strain.

taken at 2.34% and 2.99% strain, respectively. The full wave plate increased the resolution in fringe order, which enabled the length of the debond zone to be measured more accurately. The boundary between the elastic and plastic regions was not measured because the boundary was not distinct, in reality, or as seen by changes in fringe order.

Light was first transmitted at a very low value of the fringe order, which will hereto be called the birefringence limit. The birefringence length was measured from the end of the debond zone, moving away from the break, to where the pattern faded to black; this corresponded to the area where the fringe order fell below the birefringence limit. The birefringence limit was not well defined, but fell within the range from 0.01–0.05 fringe orders.

4.3.2. Measurement errors

The measurements taken from the microcomposite tapes contained uncertainties in the measurement of the length and the applied strain. The error in measuring the strain was quantified by summing the uncertainty in measuring the displacement of the clamps in the load frame, $\pm$ 0.04% strain, and the variability in the local strain at a break, nominally 3% of the applied strain. The residual was not accounted for in the calculation because its magnitude was not significant as compared to the computed error interval. The error interval for measurements in the lengths of the end separation, debond zone length, and birefringence length are described below.

The uncertainty in the measurement of the separation between the ends of the graphite fibre at breaks was due to the resolution of the micrometer eyepiece, 0.5 μm, and the difficulty in identifying the position of the end of each fibre. The combined uncertainty was roughly 1.0 μm, which translates to $\pm$ 0.15 D_c. The end separation was measured while viewing the microcomposite with unpolarized light. The observed separation pattern always contained a dark line at the midpoint between the fibre ends as seen in Fig. 10. This dark line was approximately 1.5 μm thick and restricted the measurement of the end separation to above 0.30 D_c.

The uncertainty in the length of the debond zone is mainly due to the lack of a clear distinction between the debond zone and the plastic zone. The transition between these regions took place over a region which was approximately one graphite fibre diameter, D_c, in length for strains up to 1.37%, and which grew to $4D_c$ at the highest strain level of 3.46%, still a small fraction of the debond zone.

The birefringence length had the largest uncertainty due to the lack of distinction of the edge of the debond zone and the somewhat arbitrary determination of the point at which the photoelastic pattern fades to black. The uncertainty in this measurement was roughly $\pm$ 5D_c, a small fraction of the birefringence length.

4.3.3. Summary of measurements on samples

The measurements on the break progression and the load transfer are summarized in Tables VI and VII for samples 11 and 12, respectively. The load-transfer measurements were made on only selected breaks. These breaks were selected if they were isolated to the extent that their load recovery was not affected by adjacent breaks, and if they did not lie in regions where the strain deviated markedly from the nominal strain. The number of breaks selected for averaging and the total number of breaks at a particular value of applied strain are shown in the first columns of Tables

TABLE VI Summary of the averaged measurements of the load-transfer characteristics in sample 11 as a function of strain

Selected breaks/total	Fibre end separation ($/D_c$)	Debond length ($/D_c$)	Birefringence length ($/D_c$)	Strain (%)
2/2	< 0.30	00.2	18	1.37
4/4	< 0.30	00.9	20	1.64
6/10	0.32	01.9	25	1.92
12/18	0.47	03.5	25	2.06
10/20	0.73	05.3	30	2.25
5/30	1.05	09.4	34	2.52
4/33	1.19	11.3	30	2.62
3/43	1.24	12.4	31	2.84
6/49	1.32	13.2	29	2.99
4/50	1.65	16.2	30	3.16
1/(> 50)	2.20	23.1	28	3.46

TABLE VII Summary of the averaged measurements of the load-transfer characteristics in sample 12 as a function of strain

Selected breaks/total	Fibre end separation ($/D_c$)	Debond length ($/D_c$)	Birefringence length ($/D_c$)	Strain (%)
0/1	–	–	–	2.23
4/5	0.60	06.4	27	2.34
6/8	0.82	07.7	34	2.43
6/10	1.07	09.9	34	2.60
8/16	1.18	10.6	32	2.75
12/24	1.34	12.7	33	2.89
11/29	1.50	15.6	33	3.10

VI and VII, for samples 11 and 12, respectively. The load-transfer measurements were very uniform, and consequently the measurements were averaged for all of the selected breaks at that level of strain. For example, the coefficient of variation (standard deviation/mean) was 8% for the end separation measurements made on sample 12 at 3.1% strain. This variability could have been the result of measurement error, variation in spacing and in the strain along the fibre, as well as the variability in the load-transfer properties of the graphite/epoxy interface.

5. Analysis of the graphite/epoxy load transfer data

The parameters in the constitutive model were estimated by matching the experimentally measured load-transfer characteristics as a function of applied strain to the predictions from the microcomposite shear-lag model. By selecting breaks whose load-transfer profiles were not influenced by adjacent breaks, the characteristic measurements could be averaged together, and subsequently, the analysis of the load-transfer measurements was greatly simplified. Because the residual strain was not significant, no distinction will be made in the following analysis between the applied strain and actual overall strain, ε.

5.1. Input parameters for the shear-lag solution

In order to evaluate the displacement solution of the three-fibre shear-lag problem and compare the results to the corresponding photoelastic pattern, 14 parameters had to be specified. Some of the parameters could not be determined directly, and had to be determined from a best fit of the solution to experimental results through iteration. The various parameters and the method or source used to determine their values are given below.

5.1.1. The required fibre properties

(i) Diameter of the graphite fibre, D_c. This quantity was determined using a vibroscope [25] on a fibre segment adjacent to that used in the microcomposite. The diameter of the graphite fibres in samples 11 and 12 was 5.5 μm.

(ii) Modulus of the graphite fibre, E_c. This quantity was assumed to be the constant value 278 GPa, as obtained from Hercules Corp., and was within 1% of the average value obtained from tension tests on 8 single fibres.

(iii) Stiffness of the SK glass fibres, $(AE)_g$. This quantity was measured during the proof test on each glass fibre. Fibres whose failure strains were nominally greater than 3%, were sorted by stiffness, and then pairs of near equal stiffness were used in each microcomposite. The average stiffness was 10.76 N.

5.1.2. The required constitutive parameters for the epoxy matrix in shear

(iv) Limiting elastic shear strain, γ_{yield}. This quantity was approximated from Glad [20] on similar epoxies. The limiting elastic extension ratio was 1.055, and using the relationship between shear strain and extension ratio, Equation 1, the corresponding limiting elastic shear strain, γ_{yield}, was 0.11. Admittedly this value may be an overestimate due to Poisson and

geometric effects. However, it is important to keep in mind its modelling purpose on Fig. 3. It was found that the results are insensitive to moderate deviations in this value.

(v) Shear stress in the plastic region, $\tau_{plastic}$. This quantity, taken as an average value in the plastic region, was determined from the experimental measurements on the graphite/epoxy load transfer, as described shortly.

(vi) Far-field debond shear strain, γ^*_{debond}. This quantity was determined from a fit to the experimental measurements on the graphite/epoxy load transfer, as described shortly. The far-field condition (for debonding processes far from the break) was assumed to be in effect for applied strains greater than 3.1%.

(vii) The residual shear stress in the debond zone, τ_{debond}. This quantity was calculated from the experimental measurements on the graphite/epoxy load transfer, as described shortly.

5.1.3. Several parameters for the shear-lag model of the microcomposite

(viii) Effective interfibre spacing, s. This quantity was determined by finding an average distance to the surface of the graphite fibre. This distance was estimated as the distance from the chord which equally divided the graphite fibre surface area on one-half of the graphite fibre, as shown in Fig. 13. The value of s was taken as the average for both samples and both sides of the fibre, being 3.75 μm.

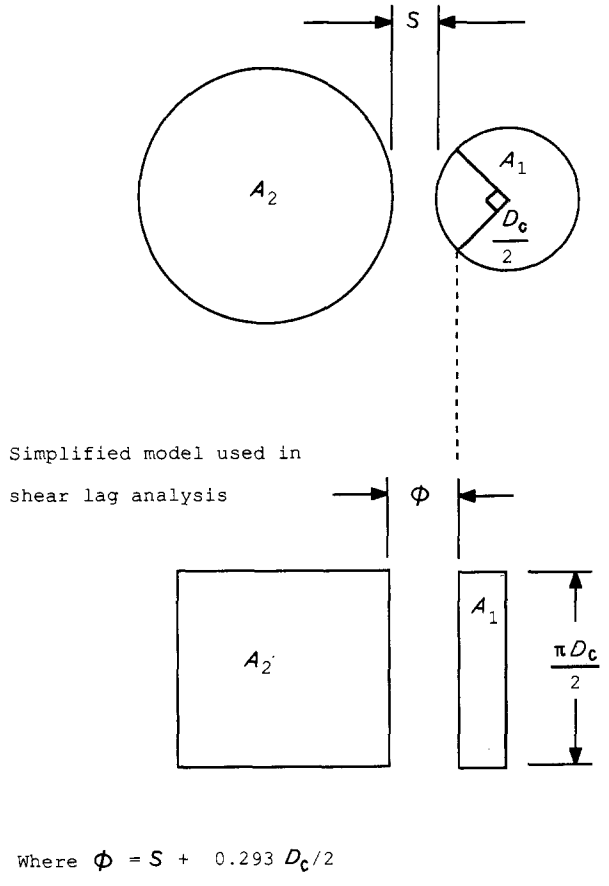

Figure 13 Determination of the effective shear spacing between the graphite and glass fibres.

(ix) Effective shear-transfer widths, h_e (elastic zone) and h_p (plastic and debond zones). This width refers to the width of the fibre over which the average shear stress between adjacent fibres is applied, a concept which originated in the shear-lag formulation. The width can be most easily evaluated in the plastic region. If we assume the matrix is perfectly plastic, then the shear width is equal to $(\pi D_c)/2$, or half of the circumference. Thus in the plastic and debond regions h_p equals $(\pi D_c)/2$. The effective shear-transfer width in the elastic region is not evaluated as easily because the shear stress is not a constant on the surface of the fibre but varies azimuthally around the fibre. To maintain continuity of the shear traction between the elastic and plastic regions, the transfer width in the elastic region was taken to be the effective transfer width in the plastic region, that is, $h_e = h_p$. Using the assumed value for the effective interfibre spacing, the effective shear-transfer width has been evaluated from experiments using an electrical analogy by Batdorf and Ko [15]. The data generated by the electrical analogy predict that the effective shear transfer width for the graphite fibre, within the configuration of the microcomposite tapes, is roughly $2D_c$, which is slightly larger than $(\pi D_c)/2$. Small variations in the value of h_e within this range have negligible effect on the determination of the parameters used to determine the constitutive behaviour of the epoxy in shear.

(x) Fibre fragment half length, L. All measurements on the graphite/epoxy load transfer were taken at breaks whose load recovery was not affected by adjacent breaks. Thus each break could be analysed as though it occurred in an infinitely long fibre. This value was determined through photoelastic observation of the breaks and confirmed by the shear-lag model of the three-fibre microcomposites. The value used was 825 μm, or 150 D_c.

5.1.4. The required photoelastic constants

(xi) Shear modulus, G. This quantity was obtained from the relationship between Young's modulus and Poisson's ratio: $G = E/[2(1 + \nu)] = 1.01$ GPa where $E = 2.80$ GPa (determined from experiment), and $\nu = 0.38$ (a typical value).

(xii) Effective thickness of the epoxy shear layer in the three-fibre microcomposites, t. This quantity was assumed to be equal to one graphite fibre diameter, D_c.

(xiii) Material fringe value, f_s. This quantity was obtained in the elastic region by measurements of the fringe order, as described in Section 2, and was found to be $f_s = 12\,690\ \mathrm{N\,m^{-1}}$. Although this value was determined in the linear elastic region of the epoxy constitutive behaviour, the deformation in the epoxy surrounding the graphite fibre was well past the elastic limit. In order to interpret the observed fringe orders, the material fringe value was converted from stress to strain using the elastic shear modulus. This value was assumed to apply to strains far in excess of the elastic limit. This assumption admittedly does not allow precise evaluation of the strain in the epoxy from the observed fringe order, and therefore, the observed values of fringe order were used only for a qualitative

comparison to the values predicted by the shear-lag analysis.

(xiv) Birefringence limit. When a small area of the epoxy is viewed through crossed polarizers, and the shear stress in that area is zero or very small, no light passes through that area. The first light is transmitted at a very low value of the fringe order, or equivalently a small value of the shear stress, which will be called the birefringence limit. The birefringence limit is not well defined, but lies within the range from 0.01–0.05 fringe orders. The distance from the area of first transmission of light to the end of the debond zone was measured and was called the birefringence length. A change in the assumed birefringence limit affects the prediction of the birefringence length by shifting its value by a constant.

5.2. Determination of the constitutive parameters of the matrix

The epoxy constitutive parameters were first estimated when the far-field conditions applied, that is when γ_{debond} is a constant and therefore equal to γ^*_{debond}, by definition. We assumed that this condition is achieved above 3.10% applied strain where debonding occurs far from the break. Above this value of applied strain, the growth of the debond zone length is a linear function of the applied strain with slope

$$\frac{\Delta\varepsilon}{\Delta L_{debond}} = \frac{4\tau_{debond}}{E_c D_c} \quad (30)$$

where ΔL_{debond} is the change in the length of the debond zone and $\Delta\varepsilon$ is the coresponding change in the strain. The slope of the debond zone length as a function of applied strain yielded the initial estimate of $\tau_{debond} = 30$ MPa.

Next the values for $\tau_{plastic}$ and γ^*_{debond}, were determined by fitting the averaged data for samples 11 and 12 for debond zone length and fibre end separation at 3.13% applied strain. Using the estimates for the constitutive parameters, the predicted value for the end separation at 3.46% applied strain was slightly high. Thus the estimate of the residual stress was reduced to $\tau_{debond} = 25$ MPa.

The constitutive parameters were again evaluated using the method described above, using the new estimate for τ_{debond}. This method produced an approximate range for the values of the four parameters used to describe the epoxy constitutive shear behaviour, as shown in Table VIII.

The necessity of reducing γ_{debond} near the fibre break can be seen in the growth of the debond zone length with applied strain as shown in Fig. 14. The data appear to be linear above 3.10% applied strain,

TABLE VIII The constitutive parameters for the epoxy in shear corresponding to the upper and lower values of the residual shear stress in the debond zone

τ_{debond} (MPa)	γ_{yield}	λ_{yield}	$\tau_{plastic}$ (MPa)	γ^*_{debond}	λ_{debond}
25	0.11	1.055	64	0.59	1.34
30	0.11	1.055	56	0.61	1.35

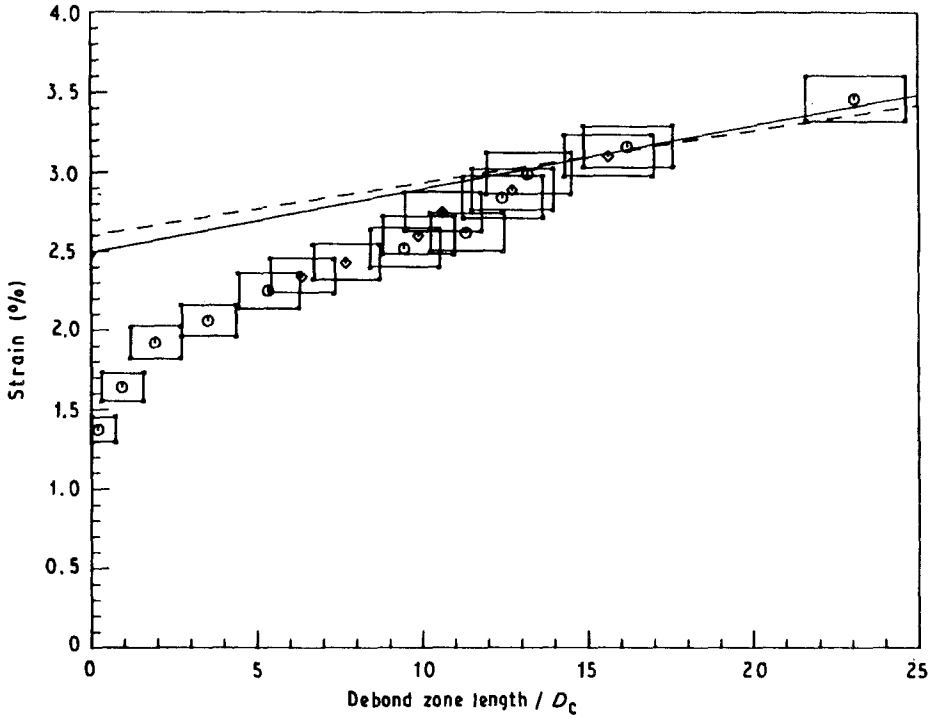

Figure 14 Comparison of the debond zone length versus strain and the experimental data, when the debond shear strain is assumed constant at all distances from the break. The boxes represent measurement uncertainty. (○) Sample 11, (◇) sample 12; (– – –) $\tau_{debond} = 25$ MPa, (——) $\tau_{debond} = 30$ MPa.

and moreover, the data as a whole cannot be fitted to a single straight line. The value of γ_{debond}, as a function of the distance from the break, was determined by matching the model to the experimental data for the debond zone length as a function of the applied strain. The fit to the experimental data for debond zone length for the two different values of τ_{debond} is shown in Fig. 15. The resulting values for γ_{debond} versus distance from the break are shown in Fig. 16. The estimated values of γ_{debond} increase quickly at first but gradually approach the far-field limit as the distance from the break becomes large. As discussed earlier, this behaviour is expected because the effect of the extensional strain would be most severe close to the break.

The fibre end separation, $2U(0)$, is shown in Fig. 17. The model is in close agreement down to 2.5% applied strain and then begins to overestimate slightly the end separation. This behaviour can be explained if the residual shear stress, in the debond zone, decreases as the fibre continues to slide past the point at which it

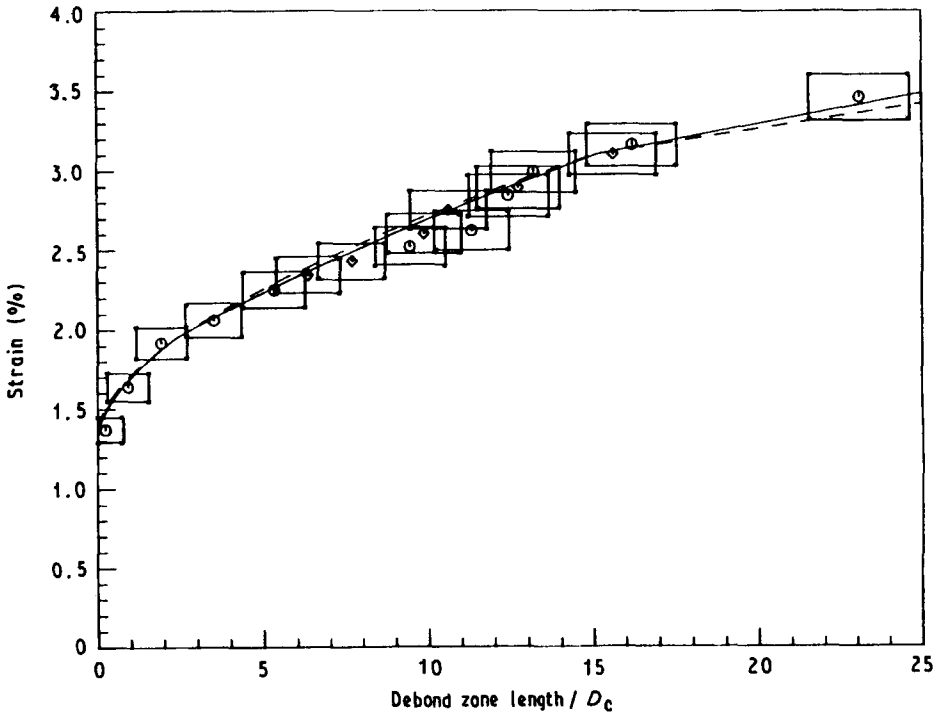

Figure 15 Comparison of computed and experimental debond zone length versus strain assuming debond shear strain is a certain function of distance from the break, which produces an excellent fit. The boxes represent measurement uncertainty. For key, see Fig. 14.

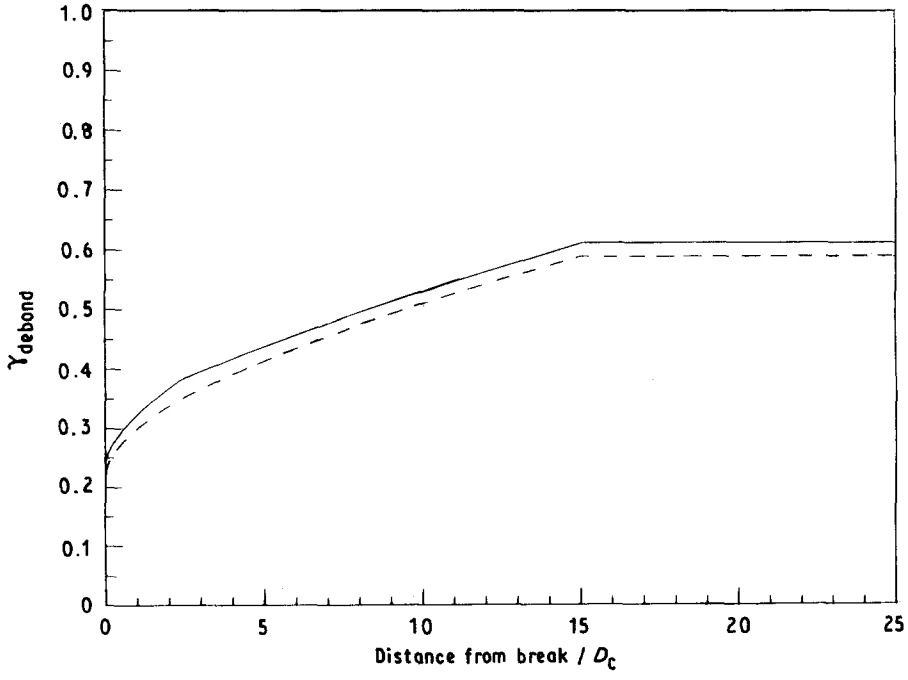

Figure 16 Plot of the resulting debond shear strain as a function of distance from the break. τ_{debond}: (---) 25 MPa, (——) 30 MPa.

debonded. Thus the average residual shear stress would be larger at lower values of the applied strain, resulting in a decrease in the fibre end separation.

The birefringence length as a function of applied strain is shown in Fig. 18. The shear-lag model is in good agreement with the experimental data. The best fit to the data resulted from the value $N = 0.02$ for the birefringence limit.

The maximum fringe order as a function of the applied strain, oberved at the transition of the plastic and debond zones (see Fig. 9), is shown in Fig. 19. The experimental data are shown as regions in fringe order and applied strain as defined by the distinct colours observed when shifted by the full wave plate. The reason for the increase in fringe order is the increase in γ_{debond} as the debond zone extends as described earlier. The predicted maximum observed fringe order is slightly less than that observed, but it should be recalled that the prediction is obtained by extrapolating the elastic birefringence behaviour into the plastic

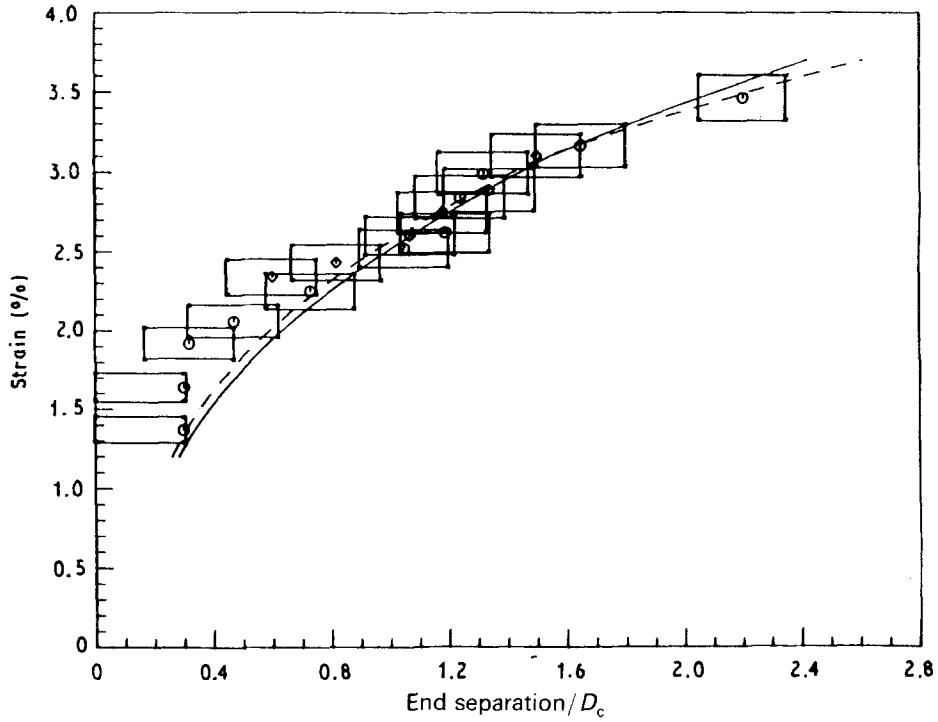

Figure 17 Comparison of experimental and computed end separation versus strain. The boxes represent measurement uncertainty. For key, see Fig. 14.

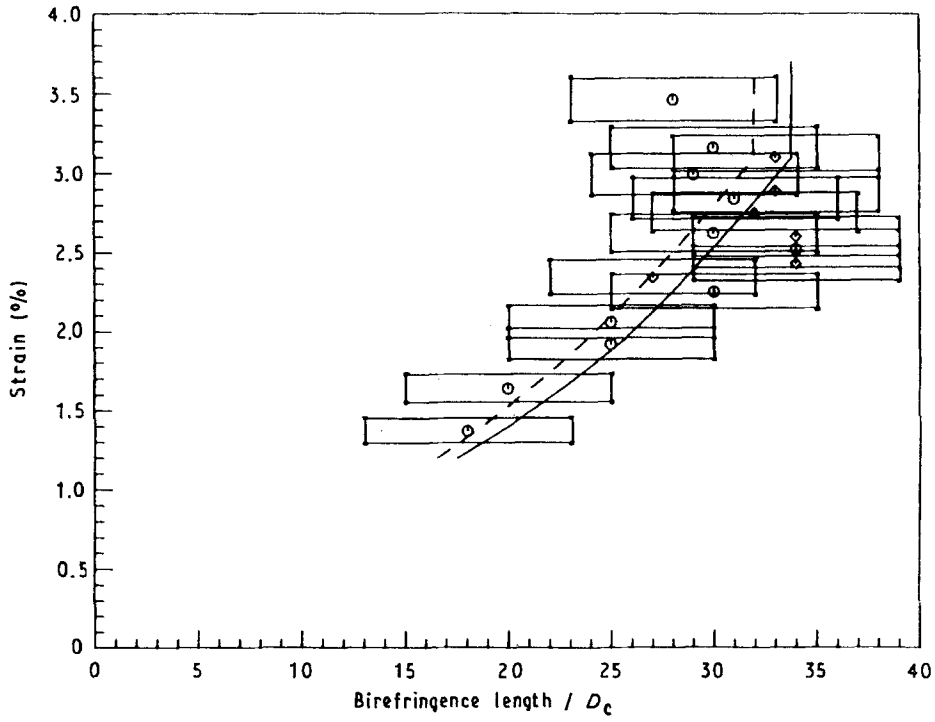

Figure 18 Comparison of experimental and computed birefringence length versus strain. Birefringence limit was 0.02 and the boxes represent measurement uncertainty. For key, see Fig. 14.

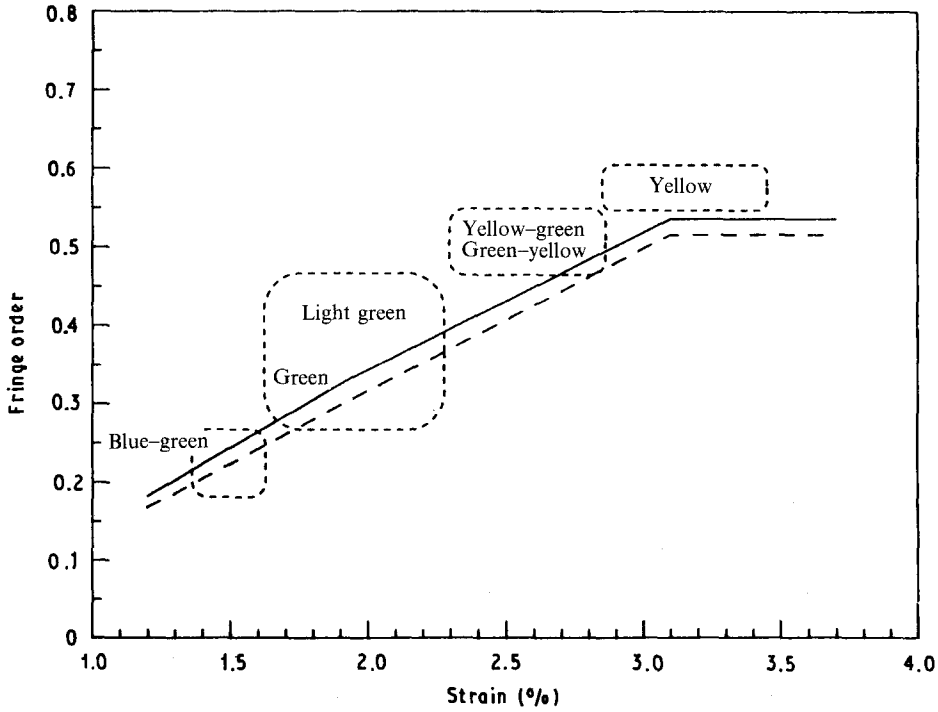

Figure 19 Comparison of model prediction of maximum fringe order versus strain and colours observed when shifted by the full wave plate. The dotted boxes indicate the range of fringe order and applied strain corresponding to the observed colours in samples 11 and 12. τ_{debond}: (– – –) 25 MPa, (——) 30 MPa.

region. It should be noted that the predicted values are in close agreement at low values of applied strain and deviate only slightly at larger values of applied strain.

5.3. Single-fibre-microcomposites

In addition to the three-fibre microcomposites, the glass fibres were omitted from one sample to assess their influence on the load transfer. This sample is similar to a single-fibre-composite but with much less matrix, and will henceforth be referred to as sample 10. In sample 10, the load from the broken graphite fibre was transmitted through shear to the surrounding matrix. The photoelastic patterns in Fig. 20 indicate that the shear profile extended across the entire width of the tape. As the strain increased, the graphite fibre began to debond along the graphite/epoxy interface, as seen in Fig. 21. Because the load transfer pattern in sample 10 was not as easily characterized as the patterns produced by the three-fibre microcomposites, only the end separation was measured. The data were not averaged, because the load transfer around some of the breaks was markedly different from that around others. The data from sample 10 are summarized in Table IX.

The increased tensile load in the surrounding matrix, due to the break in the graphite fibre, caused it to flow plastically and form a neck in the tape. The necking accelerated the debonding by decreasing the maximum possible shear strain. Two out of the six breaks experienced this debonding/necking behaviour. The tape broke at the most severely necked region, as seen in Fig. 22. (It should be noted that such necking across the entire sample for the same epoxy did not occur in the experiments of Netravali *et al.* [18] as the specimen cross-section was much larger.)

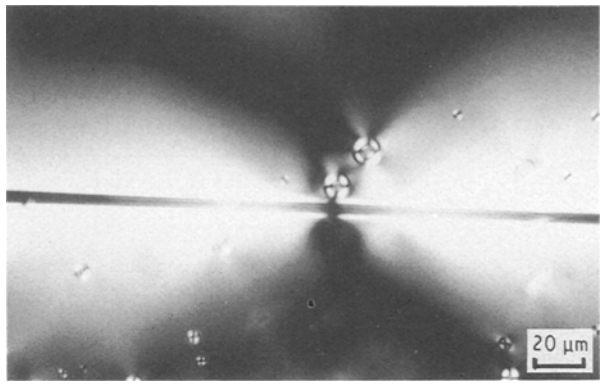

Figure 20 Shear pattern in a single-fibre-microcomposite before the epoxy had begun to yield and neck.

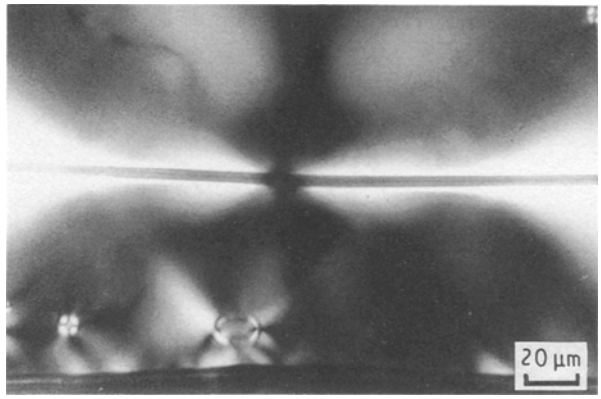

Figure 21 Shear pattern in a single-fibre-microcomposite after massive yielding at the cross-section of a fibre break.

Within the necked region, the epoxy had undergone large plastic deformation. The extent of this deformation was quantified by analysis of the plastic contraction of the necked region. The contraction was

very uniform as verified through the residual photoelastic pattern. Assuming volume-preserving plastic deformation with equal contraction through the width and the thickness, the principal extension ratios are

$$\lambda_1 = \lambda \quad (31a)$$

$$\lambda_2 = 1/\lambda^{1/2} \quad (31b)$$

$$\lambda_3 = 1/\lambda^{1/2} \quad (31c)$$

Thus by measuring the contraction through the thickness, $1/\lambda_2$, the maximum plastic extension ratio, λ_p, can be found using $\lambda_p = \lambda_1 = 1/(\lambda_2)^2$. The contraction through the thickness was 12.5% which yields $\lambda_p = 1.31$. Because the extension ratio, λ, is defined by

$$\lambda = \frac{L + \Delta L}{L} \quad (32)$$

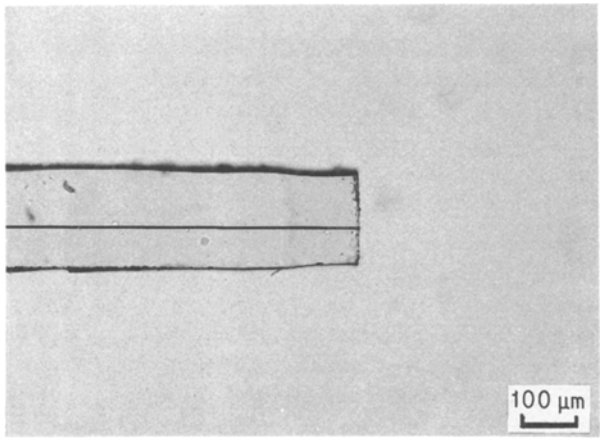

Figure 22 Necked region at fibre break which caused the sample to break.

TABLE IX Summary of the measurements of the load-transfer characteristics at single breaks in sample 10 as a function of strain

Position along fibre (mm)	Fibre end separation ($/D_c$)	Strain (%)
16.05	0.63	2.36
13.23	1.08	2.59
16.10	0.81	2.59
17.42	0.99	2.59
01.88	3.34*	2.87
11.02	0.81	2.87
12.52	1.35	2.87
13.46	1.26	2.87
16.33	1.26	2.87
17.15	1.71	2.87
17.65	8.82*	2.87

where ΔL is the change in length, and L is the initial length, then the limiting extension ratio, λ_c, is equal to the product of the yield and plastic extension ratios. Thus

$$\lambda_c = \lambda^*_{yield}\lambda_p \quad (33)$$

and using 1.055 for the yield extension ratio yields a value of the limiting extension ratio of 1.38.

6. Discussion and conclusions

The experiments verified the applicability of the shear-lag assumptions, and the necessity of incorporating elastic, plastic and debond zones to simplify the epoxy shear behaviour. In addition, they revealed that an epoxy, which behaves like a brittle material macroscopically, underwent large deformations near a fibre break. Moreover, the onset of debonding is dependent on the epoxy network structure, specifically the critical extension ratio, λ_c.

In the three-fibre microcomposites, the estimated values for the extension ratio, λ_{debond} (corresponding to γ^*_{debond} through Equation 1), and $\tau_{plastic}$ were fairly consistent with the results for λ_c and $\tau_{plastic}$ obtained by Glad [20] on thin films of a different epoxy, as given in Table X. However, λ_c would be expected to be slightly larger than the value λ_{debond} obtained from γ^*_{debond}, because debonding would occur at or before the epoxy began to fracture. From the necked section of sample 10, we earlier estimated λ_c to be about 1.38, which is in excellent agreement with the value obtained from the shear-lag analysis of the three-fibre microcomposites. The value for the average shear stress in the plastic region was slightly larger than the yield stress from Glad [20] as expected from the experimental stress–strain curve shown in Fig. 3.

Measurements made on the single-fibre microcomposite, sample 10, were consistent with the model developed for the three-fibre microcomposites. Below 2.87% nominal strain, the observed end separation was lower than in the three-fibre microcomposites. This was believed to result from a reduced initial tendency to debond due to the removal of the constraints of the glass fibres, which allowed larger values of debond shear displacements (possibly even γ^*_{debond}), and thus, shorter debond lengths for the same external strain, ε. The result was a more optimal shear profile with a shorter debond zone and a larger plastic zone. This behaviour was drastically altered as the entire cross-section began to yield (neck) at some of the breaks beyond 2.87% strain. Here the debond zones grew rapidly due to the associated sharp reduction in

TABLE X Comparison of stress/strain parameters derived from experiments on similar epoxies by Glad [20] and estimated parameters from measurements on load transfer in three-fibre microcomposites

Experiments by Glad			Microcomposites		
Thin films		Compression tests on bulk samples	M_r	λ_{debond}	$\tau_{plastic}$ (MPa)
M_r	λ_{max}	τ_{yield} (MPa)			
350	129	49	380	1.34–1.35	56–64

the permissible γ^*_{debond} associated with the sharply increased extensional strain. These results are again consistent with the proposed model.

It is interesting to compare the present results for the shear stresses on the fibre surface near a break with those obtained by Netravali *et al.* [18] on single-fibre-composites, using the same materials (though with an epoxy-compatible sizing on their graphite fibres). These authors arrived at an "average" interfacial shear stress, τ_i, = 48 MPa, where their model assumes a single, constant value over the shear transfer zone. Although this value does lie between $\tau_{plastic}$ and τ_{debond} in Table VIII, the good agreement may be somewhat fortuitous because their technique required determining, by extrapolation, the strength distribution of fibres at the length scale of the mean fragmentation length. As demonstrated in the companion paper [21], such extrapolations are prone to inaccuracies.

Second, it was observed that the value of τ_i changed only a few per cent, even though the epoxy was made flexible by the addition of polyglycol diepoxide resulting in a reduction in the bulk yield stress by a factor of 10. A likely explanation rests in a strain-hardening phenomenon similar to that observed here. In the low-modulus epoxies, small transverse penny-shaped cracks were formed at the fibre break which redistributed the tensile loads away from the break and suppressed the formation of an interface crack. Subsequently, the orientational hardening increased the shear stress at the graphite/epoxy interface above what had been seen in bulk tension tests. In contrast, an interface crack was initially formed in the high modulus epoxies which reduced the extent of the epoxy shear deformation, similar to what occurred in sample 10.

Acknowledgement

This work was supported by the Cornell University Materials Science Center, an NSF DMR-MRL.

References

1. S. B. BATDORF, *J. Reinf. Plast. Compos.* **1** (1982) 153.
2. S. L. PHOENIX and R. L. SMITH, *Int. J. Solids Struct.* **19** (1983) 479.
3. R. L. SMITH, S. L. PHOENIX, M. R. GREENFIELD, R. B. HENSTENBURG and R. E. PITT, *Proc. R. Soc. Lond.* **A388** (1983) 353.
4. B. W. ROSEN, *AIAA J.* **2** (1964) 1985.
5. N. J. WADSWORTH and I. SPILLING, *Brit. J. Appl. Phys. Ser.* 2 **1** (1968) 1049.
6. S. L. PHOENIX, P. SCHWARTZ and H. H. ROBINSON IV, *Compos. Sci. Technol.* **32** (1988) 81.
7. L. C. WOLSTENHOLME and R. L. SMITH, *J. Mater. Sci.* **24** (1989) 1559.
8. G. C. SHIH and L. J. EBERT, *J. Compos. Mater.* **21** (1987) 207.
9. J. W. MAR and K. Y. LIN, *ibid.* **13** (1979) 278.
10. J. M. WOLLA and J. G. GOREE, *ibid.* **21** (1987) 49.
11. J. M. HEDGEPETH, "Stress Concentrations in Filamentary Structures", NASA TN D-882, Langley Research Center (1961).
12. J. M. HEDGEPETH and P. van DYKE, *J. Compos. Mater.* **1** (1967) 294.
13. P. van DYKE and J. M. HEDGEPETH, *Textile Res. J.* **19** (1969) 618.
14. E. D. REEDY Jr, *J. Compos. Mater.* **19** (1985) 533.
15. S. B. BATDORF and R. W. C. KO, *AIAA J.* **23** (1985) 1749.
16. M. R. PIGGOT and D. ANDISON, *J. Reinf. Plast. Compos.* **6** (1987) 290.
17. L. S. PENN and S. M. LEE, *J. Compos. Technol. Res.* **11** (1989) 23.
18. A. N. NETRAVALI, R. B. HENSTENBURG, S. L. PHOENIX and P. SCHWARTZ, *Polym. Compos.* **10** (1989) 226.
19. R. B. HENSTENBURG and S. L. PHOENIX, *ibid.* **10** (1989) 389.
20. M. D. GLAD, PhD thesis, Cornell University, Ithaca, NY, June 1986.
21. R. GULINO and S. L. PHOENIX, *J. Mater. Sci.* **26** (1991) 3107.
22. A. E. H. LOVE, "A Treatise on the Mathematical Theory of Elasticity", 4th Edn (Dover, New York, 1927).
23. R. GULINO, PhD thesis, Cornell University, Ithaca, NY, August 1988.
24. J. W. DALLY and W. F. RILEY, "Experimental Stress Analysis" (McGraw-Hill, New York, 1978).
25. H. H. ROBINSON IV, H. F. WU, M. AMES and P. SCHWARTZ, *Rev. Sci. Instrum.* **58** (1987) 436.

Received 12 February
and accepted 3 December 1990